Electronic Properties of Ti Sites in Ziegler-Natta Catalysts

The electronic properties of the Ti sites in Ziegler-Natta catalysts

Alessandro Piovano,[a,b] Matteo Signorile,[a] Luca Braglia,[c] Piero Torelli,[c] Andrea Martini,[a,d] Toru Wada,[b,e] Gentoku Takasao,[e] Toshiaki Taniike,[b,e] Elena Groppo[a,b,*]

a) Department of Chemistry, INSTM and NIS Centre, University of Torino, Via Giuria 7, 10125 Torino, Italy

b) Dutch Polymer Institute, P.O. Box 902, 5600 AX Eindhoven, the Netherlands

c) CNR-IOM, TASC Laboratory, Trieste, Italy, 34149

d) The Smart Materials Research Institute, Southern Federal University, 344090 Sladkova 178/24 Rostov-on-Don, Russia

e) Graduate School of Advanced Science and Technology, Japan Advanced Institute of Science and Technology, 1-1 Asahidai, Nomi, Ishikawa, 923-1292, Japan

Abstract

Although Ziegler-Natta (ZN) catalysts play a major role in the polyolefins market, a true understanding of their properties at the molecular level is still missing. In particular, there is a lack of knowledge of the electronic properties of the Ti sites. Theoretical calculations predict that the electron density of the Ti sites in the pre-catalysts correlate with the activation energy for olefin insertion in the Ti-alkyl bond generated at these sites after activation by Al-alkyls. It is also well known that the effective charge on the Ti sites in the activated catalysts affects the olefin π-complexation. In this contribution we exploited two electronic spectroscopies, UV-Vis and Ti $L_{2,3}$-edge NEXAFS (the latter applied here for the first time), complemented by theoretical simulation, to investigate three ZN pre-catalysts of increasing complexity (up to an industrial system) and the corresponding catalysts activated by triethyl aluminium (TEAl). We provided compelling evidences for the presence of monomeric 6-fold coordinated Ti^{4+} species in all the pre-catalysts, which however differ in the effective charge on the Ti sites. We also unambiguously demonstrated that these sites are reduced by TEAl to two types of monomeric 5-coordinated Ti^{3+}, either alkylated or not, and that the former are involved in ethylene polymerization. In addition, small $TiCl_3$ clusters are formed in the industrial catalyst, likely due to the occurrence of severe reducing conditions within the catalyst pores. These data prove the enormous potential of these two techniques, coupled with simulation, in providing an accurate description of the electronic properties of heterogeneous ZN catalysts, which has only a few precedents in the literature.

1. Introduction

Ziegler-Natta (ZN) catalysts are at the heart of the polyolefins production, affording nowadays almost 80 million tons of polypropylene per year, with a worldwide economic turnover exceeding 100 billion dollars,[1] and their great properties are recognized as a fundamental benchmark for the whole chemical industry. Their extraordinary success in terms of activity and selectivity is due to the perfect combination of four indispensable components, namely, a titanium chloride precursor, a high surface area $MgCl_2$ support, organic molecules acting as Lewis bases (namely, the electron donors) and an aluminium alkyl activator.[2-5] The first three components constitute the pre-catalyst, which can be prepared following different routes that have been optimized in decades of industrial research[6, 7] to generate multi-grained and porous spherical particles as a result of aggregation of so-called primary particles.[8-14] This hierarchical structure is fundamental to guarantee controlled fragmentation during olefin polymerization and to provide a polymer with the desired morphology.

It is widely accepted that the primary particles are nanosized and disordered $MgCl_2$ plates (usually called δ-$MgCl_2$) whose surfaces are capped by $TiCl_4$ and electron donor molecules.[15] Following the mechanical route, $MgCl_2$ and the electron donor are ball-milled together and post-treated by $TiCl_4$: longer the grinding time, higher the surface area and the defectivity of the δ-$MgCl_2$ primary particles, which are both beneficial for the development of the catalyst activity.[16-22] When the pre-catalysts are prepared with modern chemical routes, for example through the precipitation of a $MgCl_2$ solution,[23-26] or through the solid-state conversion of $Mg(OR)_2$ precursors in the presence of $TiCl_4$ and the electron donors,[26-30] the size of the δ-$MgCl_2$ primary particles decreases by one order of magnitude and their structural disorder increases, with a concomitant increase of the catalyst performance. Besides affecting the size and the disorder of the δ-$MgCl_2$ primary particles, the synthesis protocol strongly affects their morphology, i.e. the relative extension of different surfaces. In our recent work,[31, 32] we demonstrated that the mechanical ball-milling of $MgCl_2$ favors the formation of surfaces exposing strongly acidic Mg^{2+} sites (i.e., the (110), (012) and (015) ones) at the expenses of the basal (001) one, and that the relative contribution of the (110) surface to the overall $MgCl_2$ morphology is even greater for the chemically activated ZN catalysts.

Since the structure and the morphology of the δ-$MgCl_2$ primary particles are retained during the catalyst formation in the presence of the aluminum alkyl activator, the synthetic protocol ultimately drives the distribution of the active sites and their stereo-specificity.[33-41] Albeit this concept is widely accepted based on the analysis of the polymer produced, so far direct experimental evidences on the different properties of the Ti sites in ZN catalysts have been largely

restricted. The majority of experimental data on ZN catalysts refer to the pre-catalysts or to aged catalysts, and usually provide information on either $MgCl_2$ or the electron donors, while the properties of the Ti sites are only indirectly extrapolated. One of the main aspects missing from the state-of-the-art technology in ZN catalysis is an understanding of the electronic features of the Ti sites, which in turn strongly influences the monomer insertion process. Indeed, more electron-deficient Ti active species are known to enhance both the olefin π-complexation and the agostic interaction within the α-agostic assisted Cossee-Arlman mechanism.[42] While a few recent computational studies indicate that the charge state of Ti sites in ZN pre-catalysts is sensitive to the coordination environment and correlates with the activation energy of ethylene insertion into the Ti-alkyl bond.[43, 44] A critical deficiency of experimental data mainly arises from some intrinsic difficulties which make the active sites elusive to most of the experimental techniques. Among all, the small fraction of the Ti sites (a few wt%) and their heterogeneity (i.e. co-presence of active, poorly active/dormant and inactive sites) are the most relevant ones.[45]

Herein, we provide an unprecedent contribution in the field, by thoroughly investigating the electronic properties of the Ti sites in three ZN pre-catalysts synthetized according to different protocols (whereby δ-$MgCl_2$ is obtained either by mechanical or chemical routes), and in the three related catalysts activated by triethyl aluminium, before and after ethylene polymerization, by coupling diffuse reflectance (DR) UV-Vis and Ti $L_{2,3}$-edge NEXAFS spectroscopies, complemented by theoretical simulations. Both techniques provide information on the electronic structure of the Ti sites, which in turn allow going back to their geometrical structure at the atomic scale. In more detail, absorptions in the UV-Vis range are due to the transfer of electrons from molecular orbitals mainly centred on the ligand to molecular orbitals mainly centred on Ti (charge-transfer transitions), and/or to the transfer of electrons between filled and empty d orbitals in Ti (d-d transitions), the latter being possible only for reduced Ti species.[45] On the other hand, Ti $L_{2,3}$-edge NEXAFS spectra originate from Ti(2p)→Ti(3d) electronic transitions, and act as a probe of the unoccupied valence density of states. Hence, both techniques are in principle very sensitive to the Ti-ligand interactions and able to discriminate between sites having a similar geometrical environment but yet a different electronic affinity towards the monomer. Nevertheless, DR UV-Vis spectroscopy has been only rarely used for investigating ZN catalysts,[45-52] where the spectra were not sufficiently (or properly) interpreted. As far as NEXAFS (in the soft x-ray range) is concerned, the short attenuation length of soft X-rays has long prevented the application of NEXAFS in reaction conditions, and *in situ* observations of surface reactions were limited only under the presence of gases with pressures

lower than 10^{-6} Torr. Recently, new experimental set-ups are being developing to go beyond this limitation, and a few examples of *operando* NEXAFS investigations of heterogeneous catalysts can be found in the literature.[53-62] Most of them are related to the study of supported metal oxides or metal nanoparticles, while to the best of our knowledge there are yet no examples of NEXAFS applied to ZN catalysts. Hence, the present work has a pioneering character and the ambition to demonstrate that accessing a full description of the electronic features of active sites in ZN catalysts is feasible.

2. Experimental

2.1. Samples

2.1.1. Synthesis of the pre-catalysts

A ball-milled $MgCl_2$ sample (hereafter pristine $MgCl_2$) was donated by Toho Titanium Co., Ltd., with a specific surface area (SSA) of 9.3 $m^2\ g^{-1}$, as determined by N_2 adsorption measurements. 25 g of it were filled in a 0.5 L stainless-steel pot with 235 stainless-steel balls (10 mm diameter) and subjected to planetary ball milling. The milling time was adjusted to make SSA about eight times higher, resulting into SSA of 73 $m^2\ g^{-1}$. The **$MgCl_2/TiCl_4$** pre-catalyst was prepared by titanation of the so obtained high surface area $MgCl_2$ in the presence of $TiCl_4$ vapors at 80 °C, followed by degassing at the same temperature in high vacuum, resulting in a final titanium loading close to 1.0 wt.% with respect to $MgCl_2$.

The same pristine $MgCl_2$ was also ball milled (for the same milling time) in the presence of ethylbenzoate (hereafter EB) as an electron donor at a $MgCl_2$/EB molar ratio of 16:1. The so obtained $MgCl_2$/EB sample was reacted in heptane with $TiCl_4$ at 90 °C for 2 hours, washed several times with fresh heptane, and finally dried under vacuum at 90 °C. The resulting **$MgCl_2/EB/TiCl_4$** pre-catalyst has the final Ti and EB contents of 1.0 and 6.3 wt.%, respectively.

The chemically activated ZN pre-catalyst, **ZNC(DBP)**, was prepared starting from $Mg(OEt)_2$ according to a patent[63] with slight modifications,[28, 29, 39] where n-dibuthylphthalate (hereafter DBP) was used as an internal electron donor. The Ti and DBP contents were determined as 2.6 and 14.1 wt.%, respectively.

All the samples were stored and transferred thoroughly under an inert atmosphere in order to avoid the contamination by moisture.

2.1.2. Activation of the pre-catalysts

The activation of the pre-catalysts was accomplished at room temperature by impregnating the powders with a diluted solution of triethyl aluminium (TEAl) (10 v/v% in hexane), attaining an average Al:Ti stoichiometry of 2:1. The impregnation was performed in the glove-box, directly inside the measurement cells, and the solvent was successively removed by degassing in high vacuum (DR UV-Vis) or by flowing the cell with He (NEXAFS).

2.2. Experimental methods

DR UV-vis spectra were measured with a Varian Cary5000 spectrophotometer, equipped with a diffuse reflectance sphere. The samples were measured in the powder form, in a home-made cell with a window in optical quartz (suprasil), which allows performing treatments in vacuum and/or in the presence of gases. The spectra were collected in reflectance mode and successively converted as Kubelka-Munk F(R) function.

Ti $L_{2,3}$-edges NEXAFS spectra were collected at the APE-HE beamline of the Elettra Sincrotrone Trieste facility in total electron yield (TEY) mode, which renders the measure highly surface sensitive (the probing depth being typically of a few nm). An ambient-pressure NEXAFS cell was adopted,[64] allowing to perform measurements in the presence of gases. The samples, in the powder form, were pressed inside a thin indium plate and fixed inside the cell. All the procedures were done inside a N_2-filled glove-box to prevent contamination. The cell was then inserted inside the ultra-high vacuum chamber of the APE-HE beamline, and connected to a gas line. All the measurements were performed under a 5 ml/min He flow at 1 bar. A liquid nitrogen trap was employed to remove adventitious water contaminations from the gas line. Ethylene polymerization was performed upon dosing small ethylene pulses inside the He flow. The spectra were collected with 0.1 eV energy step and 0.18 s of integration time per step. The so collected data were processed by means of THORONDOR software,[65] in order to calibrate the energy of the spectra (with reference to the 1s $\rightarrow \pi^*$ transition at 399.8 eV of nitrogen, present as Si_3N_4 in the membrane of the cell),[66] subtract the anomalous background produced by the interaction of soft X-rays with the all the crossed media (i.e., the Si_3N_4 membrane with a thickness of 100 nm,[64] and a shim of 500 µm of He gas at 1 bar), flatten the baseline of the spectra, and normalize them to the intensity of the most intense feature of the Ti L_3-edge.

2.3. Simulation of the UV-Vis and Ti $L_{2,3}$-edges NEXAFS spectra

The UV-Vis and Ti $L_{2,3}$-edges NEXAFS spectra of the pre-catalysts were simulated using the ORCA (v 4.2.1) code,[67] adopting as structural models some of the nanoclusters proposed by Takasao et al.[68]

In detail, the most stable $15MgCl_2/4TiCl_4$ models they proposed (Figures 7b and 7c in Ref. 68) were simplified by selectively removing $TiCl_x$ units. The simplified nanoclusters were re-optimized by DFT at the B3LYP level of theory,[69, 70] using the def2-TZVP as basis set.[71] Four models were considered, as shown in Figure 1: i) a Ti cation 6-fold coordinated on $MgCl_2$ (110) surface, that is so far considered the most representative picture for the Ti sites in ZN catalysts (hereafter referred to as hexa-1); ii) two 6-fold coordinated Ti species in close proximity on two intersecting $MgCl_2$ (110) surfaces (hereafter hexa-2); iii) a 5-fold coordinated Ti cation at a corner generated by the intersection of two $MgCl_2$ (104) surfaces (hereafter penta); iv) a Ti_2Cl_{2x} dimer on a $MgCl_2$ (104) surface (hereafter dimer), which in the past was considered responsible for the stereoselective propylene polymerization,[72] even though more recently its relevance has been questioned.[73-78] The atomic coordinates of the four models are provided in the SI.

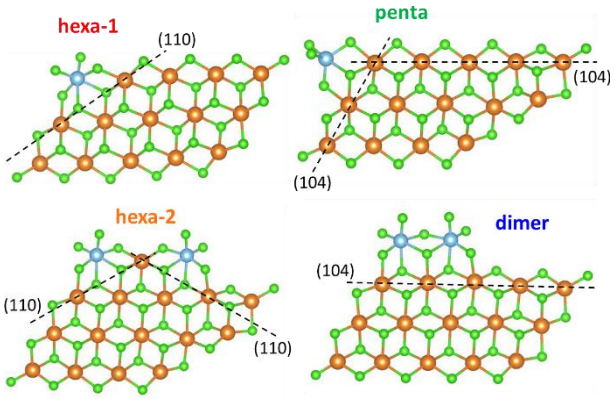

Figure 1. Four models representative of different types of $TiCl_x$ species on $MgCl_2$ clusters (Mg atoms in orange, Cl atoms in green, and Ti atoms in light blue). The models were selectively cut from the machine learning-aided structures of $TiCl_4$-capped $MgCl_2$ nanoplates determined by Takasao et al.[68] Dashed lines indicate the $MgCl_2$ surfaces involved in $TiCl_x$ chemisorption.

The hexa-1 model in Figure 1 was used as starting point for building up five models representative for the possible Ti species formed upon reaction with TEAl activator, according to the most common activation paths proposed in the literature,[2, 5] which include the formation of a coordination vacancy on the Ti site through the homolytic or heterolytic cleavage of a Cl ligand (dechlorination) and the exchange of another Cl ligand with an ethyl group (transalkylation or metathesis). The five structurally optimized models (whose atomic coordinates are provided in SI too) are represented in Figure S1 and are referred hereafter as: i) $Ti^{IV}Cl_5\oplus$, obtained from the heterolytic cleavage of a Cl ligand; ii) $Ti^{III}Cl_5$, deriving from the homolytic cleavage of a Cl; iii) $Ti^{IV}Cl_5R$,

resulting from the transalkylation; iv) $Ti^{IV}Cl_4R^{\oplus}$, obtained through a transalkylation of model $Ti^{IV}Cl_5^{\oplus}$; iv) $Ti^{III}Cl_4R$, obtained by transalkylation of model $Ti^{III}Cl_5$.

For all the optimized models described above, the UV-Vis spectra were simulated through the simplified Tamm-Dancoff formalism proposed by Grimme.[79] States up to 10 eV were considered in the calculations; all other parameters were set to the ORCA defaults. $L_{2,3}$-edge NEXAFS spectra were computed with the DFT/ROCIS method.[80] Since the L-edge transitions involve core electrons, during the NEXAFS spectra simulation relativistic corrections have been included through the ZORA formalism.[81] The orbitals involved in the Ti $L_{2,3}$ transitions were manually selected, including the Ti 2p as donor orbitals and the 100 lower energy unoccupied orbitals as acceptor ones; 100 transitions were calculated per spin state. The spin-orbit coupling correction was included in the calculations. The energy scale for simulated NEXAFS spectra has been calibrated for an improved comparison with experimental data by a multiplicative scaling factor (1.022). The latter has been obtained by comparing the simulated spectrum of $TiCl_4$ with the experimental one available from literature.[82]

3. Results and Discussion

3.1. The electronic properties of the Ti^{4+} sites in the pre-catalysts

Figure 2a shows the DR UV-Vis spectra of the three pre-catalysts, after normalization of the intensity to the most intense band for a better comparison.[83] The three spectra mostly reflect the electronic fingerprints of the $TiCl_x$ species, since bare $MgCl_2$ has no absorption in the whole UV-Vis region and the contribution of the electron donors is negligible (Figure S2). The spectra are very different from each other, implying that the electronic properties of the Ti sites in the pre-catalysts are not the same, despite the fact that the Ti^{4+} sites are expected to have the same formal oxidation state (+4), a similar coordination (6-fold coordinated) and should be surrounded mainly by chlorine ligands in all the cases.

Since Ti^{4+} has a d^0 electronic configuration, in the DR UV-Vis spectra we observe essentially the electron transfer between the filled π levels of Cl and the vacant *d* orbitals of Ti, which are split because of the crystal field effect. In the simple assumption of an octahedral coordination, the *d* orbitals of Ti are split into dt_{2g} and de_g levels, separated by the crystal-field splitting (Δ_{CF}=10Δq). Figure 2b represents a simplified molecular orbitals (MOs) diagram for a Ti^{4+} surrounded by six chlorine ligands in an octahedral field, taking into account that chlorine, as all the halides, is a π-donor ligand.[84, 85] A more rigorous MOs diagram is displayed in Figure S3. The charge-transfer (CT)

transitions observed by DR UV-Vis spectroscopy are also reported (arrows A and B in Figure 2b). Twelve *p* orbitals (two for each chlorine ligand) are available for π-bonding with the *d* orbitals of Ti^{4+}, which combine to each other to give symmetry adapted linear combination (SALC) orbitals of different symmetry. Only the t_{2g} set has any significant impact on the MO diagram, since they mix with the Ti^{4+} *d* orbitals of the same symmetry (d_{xy}, d_{xz}, d_{yz}).[84] For π-donor ligands the π-SALCs have a lower energy than the metal atomic orbitals. Hence, the bonding MOs of t_{2g} symmetry are ligand-centred and are filled, while the anti-bonding t_{2g}* π-MOs are metal-centred.[85] This effectively raises the metal dt_{2g} atomic orbitals and decreases the magnitude of Δ_{CF} with respect to the σ-bonded case. According to this scheme, the lowest energy electronic absorptions are due to transitions of the type Cl(π)→Ti(dt_{2g}) (transition A in Figure 2b and bands A' and A'' in Figure 2a) and Cl(π)→Ti(de_g) (transition B in Figure 2b and bands B in Figure 2a), respectively.[86] The experimental spectra are not constituted simply by two bands (π→dt_{2g} and π→de_g) separated by 10Δq because the Cl centred molecular orbitals are not perfectly equivalent as displayed in Figure 2b for simplicity;[84] this causes the splitting of the Cl(π)→Ti(dt_{2g}) transition into bands A' and A'' in Figure 2a. The same splitting is not observed for the Cl(π)→Ti(de_g) bands because the second component falls at higher wavenumbers, out of the measurement range.

The spectra of Ti^{4+} hexa-halides reported in the literature are characterized by a large variability in the position and in the relative intensity of the above mentioned bands, especially when spectra of compounds in the solid state are compared with those of $[TiCl_6]^{2-}$ species in solution.[87] As an example, the transmission spectrum of $[TiCl_6]^{2-}$ in acetonitrile displays the Cl(π)→Ti(dt_{2g}) transitions in the 29000 – 31850 cm^{-1} range and the Cl(π)→Ti(de_g) bands in the 38500 – 42500 cm^{-1} one, while the reflectance spectrum of solid K_2TiCl_6 shows both transitions at much lower energy, in the 23000 – 30000 cm^{-1} and 34500 – 37800 cm^{-1} intervals, respectively. The differences have been ascribed to structural variations induced by the packing of the cations in the solid state, which results in a distortion of the anions distribution (i.e. in changes as well as in the bond lengths).[87]

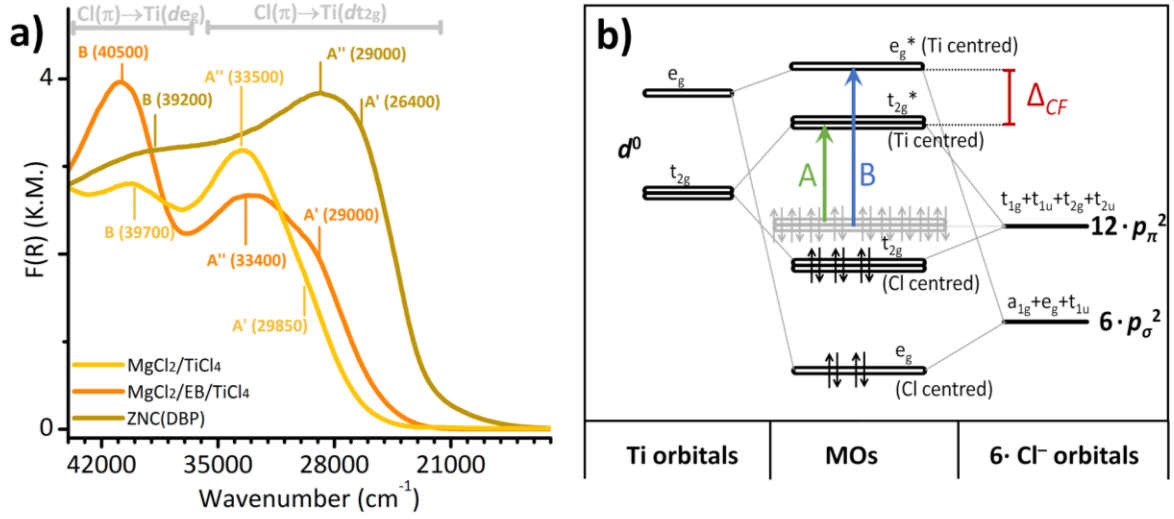

Figure 2. Part a) DR UV-Vis spectra of the three pre-catalysts. The position of the maxima of the absorption bands (evaluated at the minima of the second derivatives) are also indicated, as well as the main assignments. Part b) Simplified molecular orbitals diagram for a Ti^{4+} metal centre in an octahedral field surrounded by six σ-bonded Cl^- ligands, with a π-donor nature. The ligand-to-metal charge-transfer transitions observed by DR UV-Vis spectroscopy are also reported (arrows A and B). A more rigorous MOs diagram is reported in Figure S3.

Similar differences characterize the spectra of the three pre-catalysts reported in Figure 2a. The position of the bands observed in the DR UV-Vis spectra (evaluated as the minima in the second derivative curves) are also indicated in Figure 2a and summarized in Table 1. The spectrum of $MgCl_2/TiCl_4$ shows the first Cl(π)→Ti(dt_{2g}) transition at the highest energy (band A', 29850 cm^{-1}), but also the smallest crystal-field splitting $\Delta_{CF}(\mathrm{UV})$ (8025 cm^{-1} = 0.99 eV), where $\Delta_{CF}(\mathrm{UV})$ was evaluated as $\Delta_{CF}(\mathrm{UV}) = E(\mathrm{B}) - [E(\mathrm{A}') + E(\mathrm{A}'')]/2$, with $E(\mathrm{A}')$, $E(\mathrm{A}'')$ and $E(\mathrm{B})$ the energy position of bands A', A", and B, respectively. The spectrum of ZNC(DBP) shows the first Cl(π)→Ti(dt_{2g}) transition at the lowest energy (band A', 26400 cm^{-1}), and the largest $\Delta_{CF}(\mathrm{UV})$ (11500 cm^{-1} = 1.43 eV). The spectrum of $MgCl_2/EB/TiCl_4$ has intermediate properties, with the first Cl(π)→Ti(dt_{2g}) transition at 29000 cm^{-1} and $\Delta_{CF}(\mathrm{UV})$ = 9300 cm^{-1} = 1.15 eV, and a spectrum very similar to that reported in the literature for $[TiCl_6]^{2-}$ in acetonitrile. It is worth noting that the determination of the Δ_{CF} values from the position of the charge-transfer bands in the optical spectrum is uncommon. Usually, Δ_{CF} is estimated in a direct way from the energy position of the d-d bands only for transition metals having a d^n electronic configuration with $n \neq 0$.

Table 1. Experimentally observed bands in the DR UV-Vis and Ti $L_{2,3}$ edges NEXAFS spectra of the three pre-catalysts and their assignment. The values of the crystal-field splitting, $\Delta_{\mathbf{CF}}$, are also reported, where: $\Delta_{CF}(\mathbf{UV}) = \boldsymbol{E}(\mathbf{B}) - [\boldsymbol{E}(\mathbf{A}') + \boldsymbol{E}(\boldsymbol{A}'')]/\mathbf{2}$, $\Delta_{CF}(\mathbf{NEXAFS}) = [\boldsymbol{E}(\boldsymbol{b}\mathbf{1}) + \boldsymbol{E}(\boldsymbol{b}\mathbf{2})]/\mathbf{2} - \boldsymbol{E}(\mathbf{a})$.

Technique	Band Label	Assignment	Units	$MgCl_2/TiCl_4$	$MgCl_2/EB/TiCl_4$	ZNC(DBP)
UV-Vis	A'	Cl(π)→Ti(dt$_{2g}$)	cm^{-1}	29850	29000	26400
	A''	Cl(π)→Ti(dt$_{2g}$)	cm^{-1}	33500	33400	29000
	B	Cl(π)→Ti(de$_g$)	cm^{-1}	39700	40500	39200
		Δ_{CF}(UV)	cm^{-1}	8025	9300	11500
			eV	0.99	1.15	1.43
NEXAFS	*a*	Ti(p)→Ti(dt$_{2g}$)	eV	458.26	458.26	458.26
	b1	Ti(p)→Ti(de$_g$)	eV	459.86	459.79	460.02
	b2	Ti(p)→Ti(de$_g$)	eV	460.52	460.62	460.50
		Δ_{CF}(NEXAFS)	eV	1.93	1.94	2.00

The band assignment discussed above, based on LCAO arguments and on the assumption of an octahedral coordination for the Ti cations, is fully confirmed by the simulation of the UV-Vis spectra for the four models shown in Figure 1, which are reported in Figure S4. Even though only hexa-1 exhibits an almost perfect octahedral symmetry, all the four simulated spectra are characterized by two main bands in the 28000 – 42000 cm^{-1} region, separated by about 7000 cm^{-1} (0.87 eV), which is compatible with the experimentally determined Δ_{CF} values. The position of the Cl(π)→Ti(dt$_{2g}$) band at the lower energy is the most sensitive to the geometry of the model, spanning from about 31500 cm^{-1} for penta to about 34000 cm^{-1} for hexa-1, whereas the Cl(π)→Ti(dt$_{eg}$) band at the higher energy is almost constant for all the models at 40000 cm^{-1}. All the simulated spectra (Figure S4) are not largely different from each other, and qualitatively compatible with the experimental ones (Figure 2a). This means that UV-Vis spectroscopy is hardly usable alone to assess the structure of the Ti^{4+} sites in the three ZN pre-catalysts.

Complementary information can be obtained by analysing the Ti $L_{2,3}$-edge NEXAFS spectra of the three pre-catalysts, reported in Figure 3a after normalization to the intensity of the first feature (band a). Generally speaking, a Ti 2*p* NEXAFS spectrum originates from the $2p^6 3d^n \rightarrow 2p^5 3d^{n+1}$ electronic transition. It consists of two sets of bands representing the L_3 and L_2 edges, which correspond to the $2p_{3/2}$ and $2p_{1/2}$ excitations, respectively. Hence, the separation between the L_3 and L_2 edges is associated with the spin-orbit splitting of the 2p orbitals. For all the three pre-catalysts, the separation of the L_3 and L_2 features is 5.3 eV, which is slightly lower than the L_3-L_2 splitting observed in the Ti 2*p* NEXAFS spectrum of TiO_2 (5.5 eV)[88-90] and $FeTiO_3$ (5.4 eV).[89] Both L_3

and L_2 edges are split in two main peaks (labelled as *a* and *b*, and *c* and *d*, respectively). Within the molecular orbital picture, this separation is explained as the splitting of the Ti 3*d* molecular orbitals dictated by the symmetry of the Ti species. In the simple picture of a transition metal in octahedral symmetry, the two peaks in both the L_3 and L_2 edges are then related to electronic transitions to the dt_{2g} and de_g orbitals. Therefore, the energy difference between peaks *a* and *b* (or *c* and *d*) corresponds to the crystal field splitting $\Delta_{CF}(\mathrm{NEXAFS})$, which increases in the series $MgCl_2/TiCl_4$ < $MgCl_2/EB/TiCl_4$ < ZNC(DBP) in agreement with what was observed in the DR-UV Vis spectra, even though the absolute values are larger. This is in agreement with the literature, according to which for $10\Delta q$ values lower than 3 eV the energy splitting determined by NEXAFS is higher than the real one.[89] A comparison of $\Delta_{CF}(\mathrm{NEXAFS})$ and $\Delta_{CF}(\mathrm{UV})$ for the three pre-catalysts is shown in Figure S5.

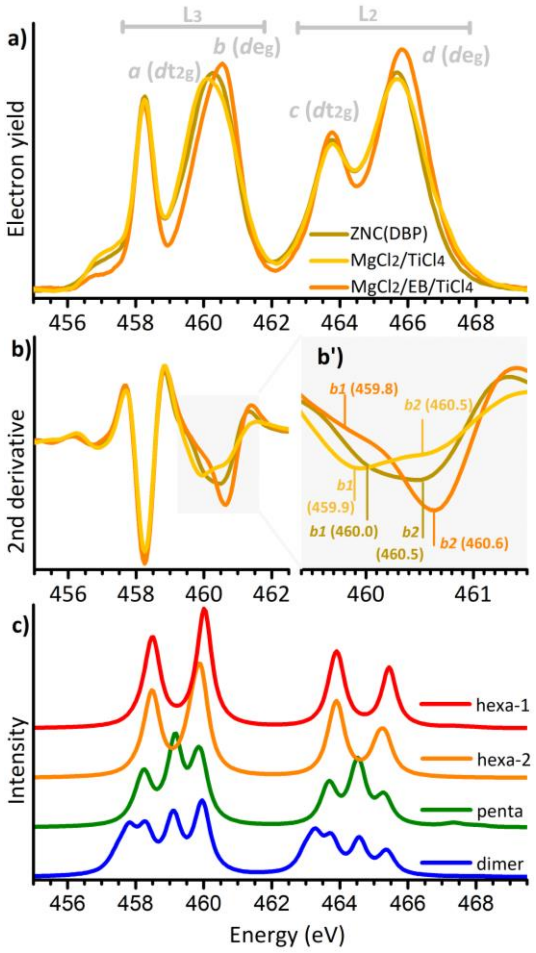

Figure 3. Part a) Experimental Ti $L_{2,3}$-edge NEXAFS spectra of the three pre-catalysts. Part b) Second derivatives of the spectra reported in part a) in the L_3 edge region; part b') reports a magnification of the second derivative signal for the de_g peak in the L_3 edge. Part c) Simulated Ti $L_{2,3}$-edge NEXAFS spectra of the four models shown in Figure 1, normalized to the number of the absorbing atoms.

Since the L_2 features are normally broadened compared to the L_3 ones because of the shorter lifetime of the $2p_{1/2}$ core-hole, we performed a detailed analysis on the L_3 edge only. The energy position of the dt$_{2g}$ and de$_g$ peaks (bands a and b in Figure 3a) are reported in Table 1. For all the three samples the de$_g$ peak is split into two main components, more evident in the second derivative curves (labelled as peaks *b1* and *b2* in Figure 3b'), indicative of at least two main families of Ti sites.[91] The larger sensitivity of the de$_g$ peak with respect to the dt$_{2g}$ one can be explained considering that the de$_g$ orbitals are oriented along the ligands σ-bonds, thus inducing a larger hybridization of those orbitals with the SALCs centred on the ligands. The origin of the splitting of the de$_g$ peak has been investigated by simulating the Ti $L_{3,2}$-edge NEXAFS spectra (Figure 3c) of the four $TiCl_x$ models described in Figure 1. The spectra of the two models containing 6-fold coordinated Ti species on the $MgCl_2$ (110) surface (structures hexa-1 and hexa-2) are very similar and well reproduce the experimental ones, with two well-defined dt$_{2g}$ and de$_g$ peaks per each L-edge. Interestingly, the dt$_{2g}$-de$_g$ split is sensitive even to small variation in the local structure of the Ti cations, and is slightly smaller for hexa-2 structure. On the other hand, the simulated spectra of penta and dimer models are much more complex than the experimentally observed ones, with the splitting of the de$_g$, and of both the de$_g$ and dt$_{2g}$ peaks, respectively.

Overall, the thorough analysis of the DR UV-Vis and Ti L_3-edge NEXAFS spectra, aided by theoretical simulation, allowed us to conclude that **the majority of the Ti sites in the three Ziegler-Natta pre-catalysts are monomeric 6-fold coordinated species, and that in all cases two main families of Ti sites characterized by slightly different structural parameters can be identified**. Nevertheless, the three pre-catalysts differ in the average crystal field splitting, Δ_{CF}. For a specific system in a certain coordination geometry, Δ_{CF} depends on both the effective oxidation state of the metal and the nature of the ligands. Upon assuming that the nature of the ligands is roughly the same for the three pre-catalysts (chlorine anions), the differences in the Δ_{CF} values determined by both techniques indicates that the *effective* oxidation state of the Ti sites is slightly different in the three cases. With reference to the schematic MOs diagram in Figure 2b, higher the *effective* oxidation state of Ti easier the electron transfer from the Cl ligands. This corresponds to a decrease of the energy of the dt$_{2g}$* molecular orbitals, and hence to an increase in the splitting energy Δ_{CF}. On these basis, the spectroscopic data reported in Figure 2 and Figure 3 and summarized in Table 1, indicate that **the Ti sites are slightly more positive in ZNC(DBP) than in $MgCl_2$/EB/$TiCl_4$ than in $MgCl_2$/$TiCl_4$**. This result is in apparent contradiction with previous findings from theoretical calculations,[76, 92] according to which the presence of electron donors nearby the Ti site should

increase the Ti electron density (and not decrease it), since the ionic nature of the system allows Ti species to electronically feel the surrounding environment in a remote fashion. Note, however, that in real systems the Ti charge reflects various factors beside the presence of donors nearby, such as the Ti/Mg ratio, as well as local surface coverage.[43] Hence, these data highlight the importance of combining theoretical accounts carried out on model systems with experimental data collected on real systems, which are inevitably more complex.

3.2. The electronic properties of the Ti sites in the activated catalysts.

After interaction with TEAl (Al:Ti=2:1) the DR UV-Vis spectra of the three pre-catalysts drastically change, as shown in Figure 4. The general behaviour is the same in the three cases, although some differences can be pointed out. For $MgCl_2/TiCl_4$ (Figure 4a) and $MgCl_2/EB/TiCl_4$ (Figure 4b), the intense band ascribed to the Cl(π)→Ti(dt$_{2g}$) charge-transfer transition upward shifts of ca. 6000 – 7000 cm^{-1}. Likely, the same happens to the band assigned to the Cl(π)→Ti(de$_g$) transition, which however shifts outside the spectral interval available with our experimental set-up. Such shift is in very well agreement with that predicted by Jørgersen by moving from a 6-fold coordinated Ti^{4+} to a 6-fold coordinated Ti^{3+} sites.[93, 94] The almost complete disappearance of the original band indicates that in both cases, in the adopted experimental conditions, **almost all the Ti^{4+} sites are reduced to Ti^{3+} by TEAl**. It is worth noticing that the spectrum of activated $MgCl_2/EB/TiCl_4$ (Figure 4b) presents two shoulders at 34600 and 29800 cm^{-1}, which are not visible in the spectrum of activated $MgCl_2/TiCl_4$ (Figure 4a). At lower wavenumbers, a weak band appears around 21500 cm^{-1} with a long tail downward extending to 13000 cm^{-1} (insets in Figure 4a and b), which is straightforwardly assigned to a Ti(dt$_{2g}$)→Ti(de$_g$) d-d transition involving monomeric Ti^{3+} sites. The energy position of this band is slightly higher than expected for a Ti^{3+} site surrounded by chlorine ligands, and might indicate the presence of an alkyl group in the Ti^{3+} coordination sphere,[95] in accordance with the spectrochemical series of the ligands.[96]

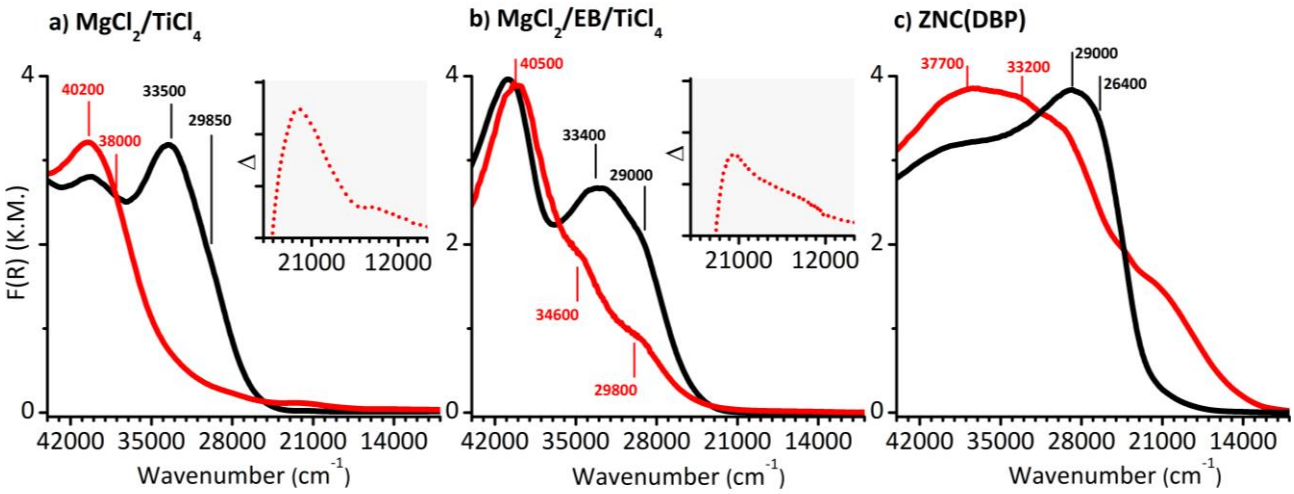

Figure 4. DR UV-Vis spectra of the three pre-catalysts before (black) and after interaction with TEAl (red), at an Al:Ti ratio of 2:1. The position of the maxima of the absorption bands (evaluated at the minima of the second derivatives) are also indicated. The insets in parts a and b report the difference spectra calculated by subtracting the spectrum of the pre-catalyst from that of the catalyst, magnified in the spectral region dominated by the d-d transition of Ti^{3+} species.

For ZNC(DBP) (Figure 4c), the evolution of the DR UV-Vis spectrum is similar but not the same. Also in this case the intense charge-transfer bands at 29000 – 26400 cm^{-1} shift upward of ca. 6000 – 7000 cm^{-1}, but the phenomenon involves only a fraction of the Ti sites. Moreover, in this case an intense and broad band appears in the lower energy region, covering the entire 24000 – 10000 cm^{-1} range. Similar absorptions have been already observed in $TiCl_3$ salts,[47, 97, 98] as described in details in Section S4. Briefly, those bands are ascribed to inter-site transitions of the type $2(3d^1) \rightarrow 3d^0+3d^2$, taking place between vicinal Ti^{3+} ions connected through a μ-Cl bridge, thus adding a partial charge-transfer character to the d-d transition, which is the reason for the high intensity.[99] Hence, the observation of those bands denote **the presence of $TiCl_3$ clusters where couples of Ti^{3+} sites exchange electrons through bridged chlorine ligands**. The presence of $TiCl_3$ clusters does not exclude the presence of monomeric Ti^{3+} sites, which however cannot be identified because their spectroscopic fingerprints are much weaker and overshadowed by those of the $TiCl_3$ clusters. The lower reducibility of the Ti^{4+} sites and the simultaneous observation of $TiCl_3$ clusters in ZNC(DBP) catalyst, not observed in the other two activated catalysts even though the activation conditions were the same, are two phenomena in apparent contradiction. They can be explained by considering that ZNC(DBP) is rich in micro- and meso-pores. Hence, a fraction of Ti sites may not be accessible by TEAl (at least until the polymer-induced fragmentation typically occurring during the olefin polymerization process), explaining the reduction at a smaller extent. At the same time, the

concentration of TEAl inside the accessible pores could cause severe reducing conditions during drying.

Figure 5 shows the Ti $L_{2,3}$-edge NEXAFS spectra of $MgCl_2$/EB/$TiCl_4$ and ZNC(DBP) before (black) and after (red) addition of TEAl. Starting the discussion from $MgCl_2$/EB/$TiCl_4$ (Figure 5a), relevant changes are observed in the Ti $L_{2,3}$-edges NEXAFS spectrum after addition of TEAl, which are better highlighted in Figure 5a', reporting the difference spectrum calculated by subtracting that of the pre-catalyst from that of the catalyst. In both the L_3 and L_2 regions new peaks appear at lower energy with respect to the bands characterizing the spectrum of the pre-catalyst. Focusing the attention on the L_3 edge, we observe the appearance of bands *a'* at 456.8 eV and *b'* at 459.2 eV (red arrows in Figure 5a') at the expenses of bands *a* and *b* (black arrows in Figure 5a'), respectively. On the basis of the literature on titanium oxides, a shift of the L_3 edge to lower energy with decreasing the oxidation state of Ti is expected, of ca. 1.7 – 2.0 eV per oxidation state.[100, 101] For mixed valence state titanium oxides, it has been demonstrated that the L_3 energy position is in between those of the end-member Ti^{3+} and Ti^{4+} compounds. Hence, we interpret these changes as due to the **conversion of a fraction of the Ti^{4+} sites into monomeric Ti^{3+},** in qualitative agreement with the DR UV-Vis results. The fact that not all the Ti^{4+} is reduced to Ti^{3+} as occurs during the DR UV-Vis experiment has to be ascribed to the different experimental set-up, which is less clean in the NEXAFS case. Hence, a fraction of TEAl might have acted as scavenger, instead than reductant. Finally, it is interesting to notice that band *b'* is much more intense than band *a'*, while the relative intensity of bands *a* and *b* in the spectrum of the pre-catalyst was almost the same. This is due to the fact that the low-lying $d t_{2g}$ orbital is half filled for a Ti^{3+} site. Hence, the probability of a Ti(2*p*)→Ti($d t_{2g}$) electronic transition is lower than for a Ti^{4+} site, where the $d t_{2g}$ orbitals are totally empty. The $d t_{2g}$-$d e_g$ crystal field splitting values for these Ti^{3+} sites as evaluated by NEXAFS is of 2.45 eV.

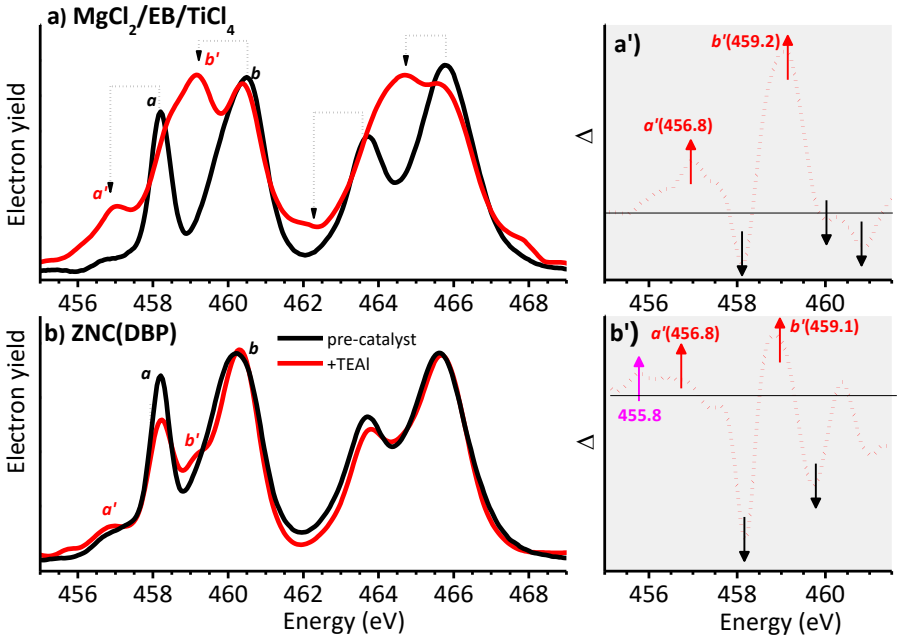

Figure 5. Part a) Ti $L_{3,2}$-edge NEXAFS spectra of the $MgCl_2$/EB/$TiCl_4$ pre-catalyst (black) and of the same after activation with TEAl, Al:Ti=2:1 (red). Part a') Difference spectrum calculated by subtracting that of the pre-catalyst from that of the catalyst, in the L_3 edge region. Parts b) and b') The same as parts a) and a') for the ZNC(DBP) sample. Arrows in parts a' and d' indicate the bands that increase (red) and decrease (black) in intensity after activation by TEAl.

For ZNC(DBP) (Figure 5b and b') much less changes are observed in the Ti $L_{2,3}$-edge NEXAFS spectrum after addition of TEAl. Only a small decrease in the intensity of bands *a* and *b* is observed (black arrows in Figure 5b'), accompanied by the appearance of weak bands at 456.8 and 459.1 eV (bands *a'* and *b'*, red arrows in Figure 5b'). Both observations indicate that in this case a small fraction of Ti^{4+} sites are reduced by TEAl to monomeric Ti^{3+} species. Nevertheless, the apparent insensitivity of the NEXAFS spectrum to the effect of TEAl has an additional explanation. According to the analysis of the DR UV-Vis spectra shown in Figure 4c, activation of ZNC(DBP) by TEAl promotes the formation of $TiCl_3$-like clusters. In this case, the NEXAFS spectrum is not expected to change dramatically, as shown in Figure S7 for $TiCl_3$ polymorphs and discussed in Section S4. This hypothesis is confirmed by the appearance of a weak band at 455.8 eV (pink arrow in Figure 5b'), which is peculiar of the violet α-form of $TiCl_3$.

In order to interpret the main features in the experimental UV-Vis and NEXAFS spectra of the activated catalysts in Figure 4 and Figure 5, we have simulated the spectra of five models representative of the possible Ti species formed upon reaction of TEAl with a monomeric 6-fold coordinated Ti^{4+} species (Figure S1). The simulated UV-Vis spectra are compared to that of the starting hexa-1 model in Figure 6a (here indicated as $Ti^{IV}Cl_6$). The spectrum of $Ti^{IV}Cl_5^{\oplus}$ shows an

intense CT band at lower energy with respect to the starting $Ti^{IV}Cl_6$, whereas experimentally the CT bands shift at higher energy upon activation by TEAl. Hence, the presence of $Ti^{IV}Cl_5^{\oplus}$-like species is discarded. On the contrary, all the other simulated UV-Vis spectra are compatible with the experimental ones. In particular, the spectrum of $Ti^{III}Cl_5$ is the one that better reproduces the experimentally observed band at 21500 cm^{-1} (d-d transition), while the spectrum of $Ti^{III}Cl_4R$ is the one that mostly accounts for the two shoulders at 34600 and 29800 cm^{-1} observed in the spectrum of the $MgCl_2$/EB/$TiCl_4$ catalyst.

Figure 6b shows the simulated NEXAFS spectra for the same models. The spectrum of $Ti^{IV}Cl_5^{\oplus}$ does not divert too much from that of $Ti^{IV}Cl_6$, with the two main features of both L edges slightly shifted at lower energies; this would be compatible with the residual bands *a* and *b* in Figure 5, but that model has been already discarded by UV-Vis spectroscopy. Both $Ti^{IV}Cl_4R^{\oplus}$ and $Ti^{IV}Cl_5R$ models display a third feature per L edge at higher energy, not compatible with the experimental spectra, so that the presence of those Ti species in the activated catalysts is excluded. Finally, $Ti^{III}Cl_5$ and $Ti^{III}Cl_4R$ models have NEXAFS signals quite complex and similar to each other. Both spectra show four bands for each L edge, shifted at lower energy with respect to the spectrum of the starting $Ti^{IV}Cl_6$ model, which account well for the experimentally observed bands *a'* and *b'* (in particular *a'* is very well reproduced by $Ti^{III}Cl_4R$ model).

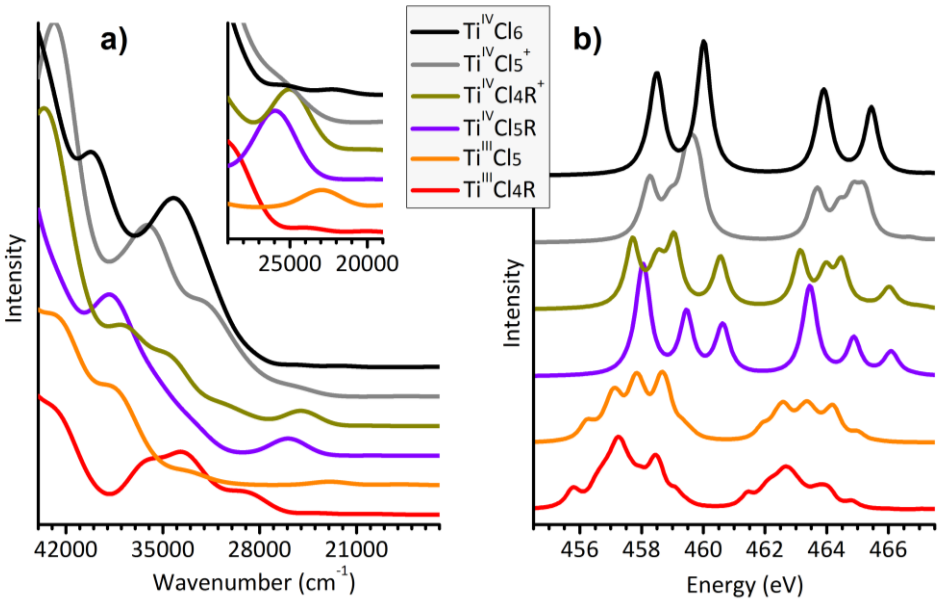

Figure 6. Simulated UV-Vis (part a) and Ti $L_{2,3}$-edge NEXAFS (part b) spectra for five models (Figure S1) representative of the possible Ti species formed upon reaction of TEAl with the hexa-1 model (here labelled as $Ti^{IV}Cl_6$).

All in all, the experimental DR UV-Vis and NEXAFS data coupled with DFT simulation clearly indicate that **the majority of the Ti sites in $MgCl_2/TiCl_4$ and $MgCl_2$/EB/$TiCl_4$ are reduced by TEAl mostly to monomeric penta-coordinated $Ti^{III}Cl_5$ species, but also at a minor extent to alkylated $Ti^{III}Cl_4R$ ones**. In **ZNC(DBP), instead, TEAl promotes the formation of small $TiCl_3$ clusters** (i.e. species where couples of Ti^{3+} sites share a bridged Cl ligand), whose contribution dominates the UV-Vis spectrum. Nevertheless, NEXAFS reveals that also in this case **a minor amount of monomeric Ti^{3+} species** is formed.

3.3. Identification of the active sites: in situ ethylene polymerization.

The experimentally detected $Ti^{III}Cl_4R$ sites satisfy all the conditions required by the Cossee-Arlman mechanism to be active in ethylene polymerization,[42] while the $Ti^{III}Cl_5$ species, being not alkylated, are not expected to participate to it. To demonstrate the involvement of the former in the ethylene polymerization reaction, we measured the DR UV-Vis and NEXAFS spectra after/during the initial stages of ethylene polymerization under very mild conditions, representative of pre-polymerization conditions adopted in industrial processes. Upon ethylene insertion into the Ti^{III}–R bond we do not expect relevant changes in the electronic features of the active sites, since a polymeryl chain is not dissimilar from the alkyl group R. Nevertheless, at the initial stages of the reaction, the formed PE has the capability to selectively mask the active sites. In DR UV-Vis spectroscopy this happens because the polymer locally changes the scattering properties of the catalyst,[102] while in TEY-NEXAFS the insulating polymer chains attenuate the photo-electrons escaping from the absorbing Ti atoms (i.e. the active sites). The net result is that, when comparing the spectra collected before with those collected after/during ethylene polymerization, an erosion of a few bands should be observed in the latter: the bands affected by the reaction will be associated to the sites involved in polymer formation, while those unaffected will be ascribed to the sites not involved in the polymerization.

Figure 7 shows the evolution of the DR UV-Vis and Ti $L_{2,3}$-edge NEXAFS spectra upon ethylene polymerization on the $MgCl_2$/EB/$TiCl_4$ catalyst activated by TEAl. An analogous sequence has been obtained for the TEAl-activated ZNC(DBP) catalyst, as reported in Figure S8. In the DR UV-Vis spectrum (Figure 7a), ethylene polymerization (testified by the appearance in the NIR region of the PE fingerprints grown over the signals of the alkyl groups already present in the catalyst, inset) causes the selective erosion of the bands at 34600 and 29800 cm^{-1}, which can thus be ascribed to

the Ti sites involved in the catalysis. It is worth recalling that the simulated spectrum better accounting for those two bands is the spectrum of the $Ti^{III}Cl_4R$ model (Figure 6).

In the NEXAFS experiment (Figure 7b), ethylene polymerization was carried out by sending ethylene pulses on the catalyst and collecting a spectrum after each pulse. Noteworthy, the total intensity of the NEXAFS spectra decreases along with the sequence, but bands *a'* and *b'* decrease faster than bands *a* and *b*. This is well evident by looking to the difference spectrum in Figure 7b', which was calculated by subtracting the spectrum of the catalyst from that measured after the first ethylene pulse. The overall decrease in intensity is associated with the formation of a layer of polyethylene on all the catalyst particles. However, the bands ascribed to monomeric Ti^{3+} sites are those decreasing faster (and basically the only ones affected after the first ethylene pulse). The sequence of NEXAFS spectra indicate that **a consistent fraction of the monomeric Ti^{3+} sites are active in ethylene polymerization**. A similar behaviour is observed for the ZNC(DBP) catalyst (Figure S8b), where however the decrease of bands *a'* and *b'* is less evident, being the NEXAFS spectrum dominated by the unreactive $TiCl_3$-like clusters.

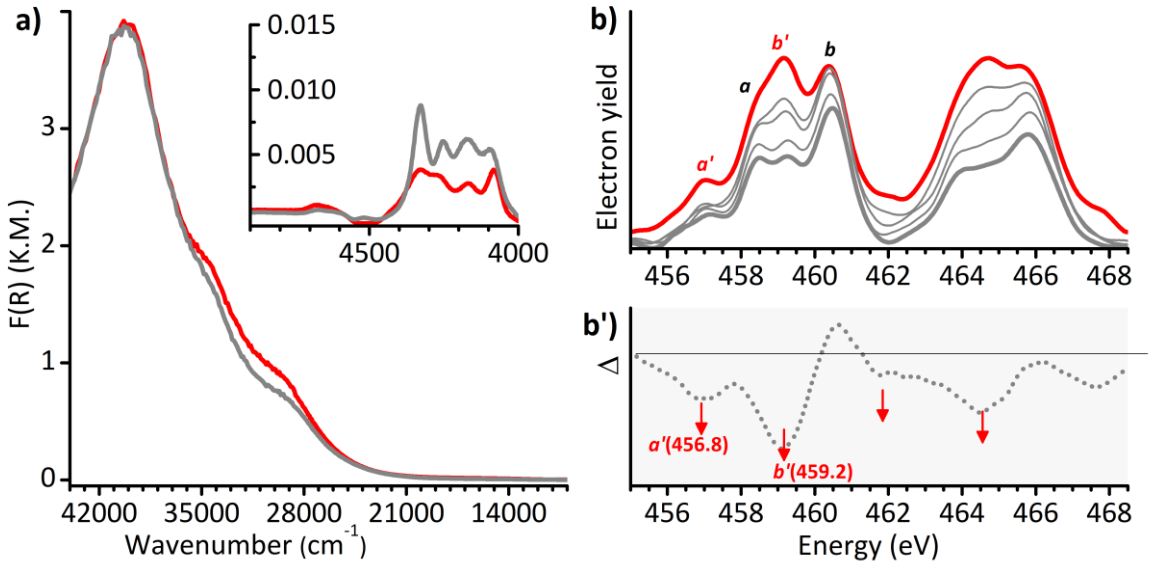

Figure 7. DR UV-Vis (part a) and Ti $L_{3,2}$-edge NEXAFS (part b) spectra of the $MgCl_2$/EB/$TiCl_4$ catalyst activated by TEAl, Al:Ti=2:1 (red) and evolution of the spectra upon addition of ethylene in the reaction cell (grey). The inset in part a displays a magnification of the NIR region. Part b') Difference spectrum calculated by subtracting that of the catalyst from the first one collected after ethylene polymerization. Arrows in part b' indicate the bands that decrease in intensity after activation by TEAl.

4. Conclusions

In this contribution we reported a thorough characterization of the electronic properties of the Ti sites in three ZN pre-catalysts with an increasing degree of complexity, and in the corresponding catalysts obtained upon activation with TEAl. In particular, we have analysed two model samples ($MgCl_2/TiCl_4$ and $MgCl_2$/EB/$TiCl_4$) and an industrial-like one (ZNC(DBP)). DR UV-Vis and Ti $L_{2,3}$-edge NEXAFS spectroscopies, combined with theoretical calculations, provided compelling evidences for the presence of monomeric 6-fold coordinated Ti^{4+} species in all the three pre-catalysts, categorized in at least two main families characterized by slightly different structural parameters. In particular, the experimental data are compatible with $Ti^{IV}Cl_6$ species on $MgCl_2$ (110) or equivalent surfaces, but also with the structure proposed by Cavallo and co-workers,[41] which originates from chemisorption of $TiCl_4$ at a step defect on the thermodynamically more stable (104) surface. Ti_2Cl_{2x} dimers and 5-fold coordinated Ti^{4+} species have been discarded, since their spectroscopic fingerprints are not compatible with the experimental data. The observation of well-defined monomeric sites in heterogeneous ZN pre-catalysts and in particular in the industrial one is remarkable by itself, considering the complexity of the catalyst formulation. Moreover, DR UV-Vis and Ti $L_{2,3}$ NEXAFS spectra allowed us to estimate the crystal-field splitting between the d orbitals of Ti, and from there the *effective* positive charge on the Ti sites, which is different in the three pre-catalysts and higher in the industrial one. Determining experimentally the effective charge state of the Ti^{4+} sites in ZN pre-catalysts is relevant for catalysis, because it correlates with the activation energy for olefin insertion into the Ti-alkyl bond formed after activation.

After activation by TEAl, the majority of the Ti^{4+} sites in the two model catalysts are reduced to monomeric 5-coordinated Ti^{3+} sites, either in the form $Ti^{III}Cl_5$ (i.e. with a coordination vacancy, but not alkylated) or in the form $Ti^{III}Cl_4R$ (i.e. with both a coordination vacancy and an alkyl group). The latter, less abundant, are the sites involved in ethylene polymerization, as demonstrated by experiments performed in the presence of ethylene. In the industrial catalyst, instead, TEAl reduces only a fraction of the Ti^{4+} sites, forming both monomeric 5-coordinated $Ti^{III}Cl_4R$ species active in ethylene polymerization, and small inactive $TiCl_3$-like clusters. The lower reducibility of the Ti^{4+} sites and the co-presence of $TiCl_3$ clusters is explained by considering the porous nature of the industrial catalyst. It is worth noticing that, although Ti^{III}-alkyl species have been proposed long time ago as key intermediates in olefin polymerization, their unambiguous characterization has represented one of the main challenges in the last sixty years. Recently, pulse EPR spectroscopy combined with DFT calculations was adopted to characterize in details molecular and supported Ti^{III}-alkyl

complexes,[103, 104] as well as industrial ZN catalysts,[105, 106] providing structural details which are in good agreement with our findings.

The present work has prompted the development of new experimental set-ups and theoretical methodologies to fully exploit the potentials of two electronic spectroscopies, UV-Vis and NEAFS, in providing direct information on the nature of the Ti sites in ZN pre-catalysts, on their changes in the presence of the aluminium-alkyl activator and during ethylene polymerization. Both methods allow to detect all the Ti sites present in the samples at each catalytic stage, at the same time discriminating between active and inactive species. The application of these techniques to a platform of ZN catalysts of industrial interest in different conditions will represent a new powerful tool for disclosing the blackbox of the ZN catalytic process, even under reaction conditions.

Acknowledgements

The work of A.P., T.W., T.T. and E.G. forms part of the research program of DPI, project #802. The work of A.M., L.B. and P.T. forms part of project n. 2017KKP5ZR PRIN-2017 MOSCATo. The work of G.T. was supported by JSPS KAKENHI Grant Number JP20J15042. The authors acknowledge the C3S consortium for granting computational resources on the OCCAM cluster, funded by the Compagnia di San Paolo. This work has been partly performed in the framework of the Nanoscience Foundry and Fine Analysis (NFFA-MIUR Italy Progetti Internazionali) facility. The NEXAFS experiments could not have been performed without the inspiration and strong support of our beloved Carlo Lamberti, who strongly believed to the potential of the method since the beginning, despite many discouraging results during the initial beamtimes. This work is the consecration of his efforts.

REFERENCES and NOTES

(1) Baker, I., Polypropylene. In *Fifty Materials That Make the World.*, Springer, Cham: 2018.

(2) Albizzati, E.; Giannini, U.; Collina, G.; Noristi, L.; Resconi, L., Catalysts and polymerizations. In *Polypropylene Handbook*, Moore, E. P. J., Ed. Hanser-Gardner Publications: Cincinnati (Ohio, USA), 1996.

(3) Busico, V., Giulio Natta and the Development of Stereoselective Propene Polymerization. In *Polyolefins: 50 years after Ziegler and Natta I*, Kaminsky, W., Ed. Springer: Berlin, 2013; Vol. 257, pp 37-57.

(4) Stürzel, M.; Mihan, S.; Mülhaupt, R., From Multisite Polymerization Catalysis to Sustainable Materials and All-Polyolefin Composites. *Chem. Rev.* **2016,** *116* (3), 1398-1433.

(5) Kumawat, J.; Gupta, V. K., Fundamental aspects of heterogeneous Ziegler-Natta olefin polymerization catalysis: an experimental and computational overview. *Polym. Chem.* **2020,** *11* (38), 6107-6128.

(6) Galli, P.; Vecellio, G., Technology: driving force behind innovation and growth of polyolefins. *Prog. Polym. Sci.* **2001,** *26* (8), 1287-1336.

(7) Busico, V.; Cipullo, R.; Mingione, A.; Rongo, L., Accelerating the Research Approach to Ziegler-Natta Catalysts. *Ind. Eng. Chem. Res.* **2016,** *55* (10), 2686-2695.

(8) Noristi, L.; Marchetti, E.; Baruzzi, G.; Sgarzi, P., Investigation on the particle growth mechanism in propylene polymerization with MgCl2-supported ziegler-natta catalysts. *J. Polym. Sci., Part A: Polym. Chem.* **1994,** *32* (16), 3047-3059.

(9) Busico, V.; Causà, M.; Cipullo, R.; Credendino, R.; Cutillo, F.; Friederichs, N.; Lamanna, R.; Segre, A.; Van Axel Castelli, V., Periodic DFT and high-resolution magic-angle-spinning (HR-MAS) H-1 NMR investigation of the active surfaces of MgCl2-supported Ziegler-Natta catalysts. The MgCl2 matrix. *J. Phys. Chem. C* **2008,** *112* (4), 1081-1089.

(10) Taniike, T.; Thang, V. Q.; Binh, N. T.; Hiraoka, Y.; Uozumi, T.; Terano, M., Initial Particle Morphology Development in Ziegler-Natta Propylene Polymerization Tracked with Stopped-Flow Technique. *Macromol. Chem. Phys.* **2011,** *212* (7), 723–729.

(11) Taniike, T.; Funako, T.; Terano, M., Multilateral characterization for industrial Ziegler-Natta catalysts toward elucidation of structure-performance relationship. *J. Catal.* **2014,** *311*, 33-40.

(12) Blaakmeer, E. S.; Antinucci, G.; Busico, V.; Van Eck, E. R. H.; Kentgens, A. P. M., Solid-State NMR Investigations of MgCl2 Catalyst Support. *J. Phys. Chem. C* **2016,** *120* (11), 6063-6074.

(13) Chammingkwan, P.; Terano, M.; Taniike, T., High-Throughput Synthesis of Support Materials for Olefin Polymerization Catalyst. *ACS Comb. Sci.* **2017,** *19* (5), 331–342.

(14) Breuza, E.; Antinucci, G.; Budzelaar, P. H. M.; Busico, V.; Correa, A.; Ehm, C., MgCl2-Supported Ziegler-Natta Catalysts: a DFT-D "Flexible-Cluster" Approach to Internal Donor Adducts. *J. Phys. Chem. C* **2018,** *122* (16), 9046-9053.

(15) Taniike, T.; Terano, M., Adv. Polym. Sci. *The Use of Donors to Increase the Isotacticity of Polypropylene* **2013,** *257*, 81-98.

(16) Bart, J. C. J., Activation of Magnesium Chloride by Dry Milling. *J. Mater. Sci.* **1993,** *28* (1), 278-284.

(17) Delogu, F.; Mulas, G.; Schiffini, L.; Cocco, G., Mechanical work and conversion degree in mechanically induced processes. *Mater. Sci. Eng., A* **2004,** *382* (1), 280-287.

(18) Galli, P.; Barbé, P. C.; Guidetti, G.; Zannetti, R.; Marigo, A.; Bergozza, M.; Fichera, A., The activation of MgCl2-supported Ziegler-Natta catalysts: A structural investigation. *Eur. Polym. Chem.* **1983,** *19*, 19-24.

(19) Noristi, L.; Barbè, P. C.; Baruzzi, G., Effect of the internal/external donor pair in high-yield catalysts for propylene polymerization, 1. Catalyst-cocatalyst interactions. *Makromol. Chem.* **1991,** *192* (5), 1115-1127.

(20) Soga, K.; Ohgizawa, M.; Shiono, T., Copolymerization of ethylene and propene with a TiCl4/MgCl2-Al(C2H5)3 catalyst system using a stopped-flow method. *Makromol. Chem.* **1993,** *194* (8), 2173-2181.

(21) Brambilla, L.; Zerbi, G.; Nascetti, S.; Piemontesi, F.; Morini, G., Experimental and Calculated Vibrational Spectra and Structure of Ziegler-Natta Catalyst Precursor: 50/1 Comilled MgCl2-TiCl4. *Macromol. Symp.* **2004,** *213*, 287-301.

(22) Brambilla, L.; Zerbi, G.; Piemontesi, F.; Nascetti, S.; Morini, G., Structure of MgCl2-TiCl4 complex in co-milled Ziegler-Natta catalyst precursors with different TiCl4 content: Experimental and theoretical vibrational spectra. *J. Mol. Catal. A-Chem.* **2007,** *263* (1-2), 103-111.
(23) Chung, J. S.; Song, I. K.; Lee, W. Y.; Park, H. M., Morphology control of a MgCl2-supported Ziegler-Natta catalyst by the recrystallization method. *Macromol. Chem. Phys.* **1995,** *196* (4), 1205-1210.
(24) Choi, J. H.; Chung, J. S.; Shin, H. W.; Song, I. K.; Lee, W. Y., The effect of alcohol treatment in the preparation of MgCl2 support by a recrystallization method on the catalytic activity and isotactic index for propylene polymerization. *Eur. Polym. J.* **1996,** *32* (4), 405-410.
(25) Parada, A.; Rajmankina, T.; Chirinos, J., Study of the MgCl2 recrystallization conditions on Ziegler-Natta catalyst properties. *Polym. Bull.* **1999,** *43* (2), 231-238.
(26) Piyavit, P.; Piyasan, P., Comparison of Activity of Ziegler-Natta Catalysts Prepared by Recrystallization and Chemical Reaction Methods towards Polymerization of Ethylene. *Eng. J.* **2009,** *13* (1), 57-64.
(27) Lee, D. H.; Jeong, Y. T.; Soga, K., In situ formation of magnesium chloride support and internal donor during preparation of propylene polymerization catalysts. *Ind. Eng. Chem. Res.* **1992,** *31* (12), 2642-2647.
(28) Dashti, A.; Ramazani Sa, A.; Hiraoka, Y.; Kim, S. Y.; Taniike, T.; Terano, M., Kinetic and morphological study of a magnesium ethoxide-based Zieglerâ€“Natta catalyst for propylene polymerization. *Polym. Int.* **2009,** *58* (1), 40-45.
(29) Funako, T.; Chammingkwan, P.; Taniike, T.; Terano, M., Alternation of Pore Architecture of Ziegler-Natta Catalysts through Modification of Magnesium Ethoxide. *Macromol. React. Eng.* **2015,** *9* (4), 325-332.
(30) Klaue, A.; Kruck, M.; Friederichs, N.; Bertola, F.; Wu, H.; Morbidelli, M., Insight into the Synthesis Process of an Industrial Ziegler-Natta Catalyst. *Ind. Eng. Chem. Res.* **2019,** *58* (2), 886-896.
(31) Wada, T.; Takasao, G.; Piovano, A.; D'Amore, M.; Thakur, A.; Chammingkwan, P.; Bruzzese, P. C.; Terano, M.; Civalleri, B.; Bordiga, S.; Groppo, E.; Taniike, T., Revisiting the identity of δ-MgCl2: Part I. Structural disorder studied by synchrotron X-ray total scattering. *J. Catal.* **2020,** *submitted*.
(32) Piovano, A.; D'Amore, M.; Wada, T.; Bruzzese, P. C.; Takasao, G.; Thakur, A.; Chammingkwan, P.; Terano, M.; Civalleri, B.; Bordiga, S.; Taniike, T.; Groppo, E., Revisiting the identity of δ-MgCl2: Part II. Morphology and exposed surfaces studied by vibrational spectroscopies and DFT calculation. *J. Catal.* **2020**.
(33) Busico, V.; Corradini, P.; De Martino, L.; Proto, A.; Savino, V.; Albizzati, E., Polymerization of propene in the presence of MgCl2-supported Ziegler-Natta catalysts, 1. The role of ethyl benzoate as “internal” and “external” base. *Makromol. Chem.* **1985,** *186* (6), 1279-1288.
(34) Iiskola, E.; Pelkonen, A.; Kakkonen, H. J.; Pursiainen, J.; Pakkanen, T. A., A novel MgCl2-supported Ziegler-Natta catalyst composition: Stereospecific polymerization of propene without external donor. *Makromol. Chem., Rapid Commun.* **1993,** *14* (2), 133-137.
(35) Liu, B.; Nitta, T.; Nakatani, H.; Terano, M., Specific Roles of Al-Alkyl Cocatalyst in the Origin of Isospecificity of Active Sites on Donor-Free TiCl4/MgCl2 Ziegler-Natta Catalyst. *Macromol. Chem. Phys.* **2002,** *203* (17), 2412-2421.
(36) Corradini, P.; Guerra, G.; Cavallo, L., Do New Century Catalysts Unravel the Mechanism of Stereocontrol of Old Ziegler-Natta catalysts? *Acc. Chem. Res.* **2004,** *37* (4), 231-241.
(37) Busico, V.; Cipullo, R.; Pellecchia, R.; Ronca, S.; Roviello, G.; Talarico, G., Design of stereoselective Ziegler-Natta propene polymerization catalysts. *Proc. Natl. Acad. Sci.* **2006,** *103* (42), 15321-15326.
(38) Correa, A.; Piemontesi, F.; Morini, G.; Cavallo, L., Key Elements in the Structure and Function Relationship of the MgCl2/TiCl4/Lewis base Ziegler-Natta Catalytic System. *Macromol.* **2007,** *40* (25), 9181-9189.
(39) Hiraoka, Y.; Kim, S. Y.; Dashti, A.; Taniike, T.; Terano, M., Similarities and Differences of the Active Sites in Basic and Advanced MgCl2-Supported Ziegler-Natta Propylene Polymerization Catalysts. *Macromol. React. Eng.* **2010,** *4* (8), 510-515.
(40) Correa, A.; Credendino, R.; Pater, J. T. M.; Morini, G.; Cavallo, L., Theoretical Investigation of Active Sites at the Corners of MgCl2 Crystallites in Supported Zieglerâ€“Natta Catalysts. *Macromolecules* **2012,** *45* (9), 3695-3701.

(41) Credendino, R.; Liguori, D.; Fan, Z.; Morini, G.; Cavallo, L., Toward a Unified Model Explaining Heterogeneous Ziegler-Natta Catalysis. *ACS Catal.* **2015,** *5* (9), 5431-5435.
(42) Cossee, P., Ziegler-Natta catalysis I. Mechanism of polymerization of α-olefins with Ziegler-Natta catalysts. *J. Catal.* **1964,** *3* (1), 80-88.
(43) Takasao, G.; Wada, T.; Thakur, A.; Chammingkwan, P.; Terano, M.; Taniike, T., Insight into structural distribution of heterogeneous Ziegler–Natta catalyst from non-empirical structure determination. *J. Catal.* **2021,** *394*, 299-306.
(44) Bahri-Laleh, N.; Hanifpour, A.; Mirmohammadi, S. A.; Poater, A.; Nekoomanesh-Haghighi, M.; Talarico, G.; Cavallo, L., Computational modeling of heterogeneous Ziegler-Natta catalysts for olefins polymerization. *Prog. Polym. Sci.* **2018,** *84*, 89-114.
(45) Groppo, E.; Seenivasan, K.; Barzan, C., The potential of spectroscopic methods applied to heterogeneous catalysts for olefin polymerization. *Catal. Sci. Technol.* **2013,** *3*, 858-878.
(46) Seenivasan, K.; Sommazzi, A.; Bonino, F.; Bordiga, S.; Groppo, E., Spectroscopic Investigation of Heterogeneous Ziegler-Natta Catalysts: Ti and Mg Chloride Tetrahydrofuranates, Their Interaction Compound, and the Role of the Activator. *Chem. Eur. J* **2011,** *17* (31), 8648-8656.
(47) Groppo, E.; Gallo, E.; Seenivasan, K.; Sommazzi, A.; Bordiga, S.; Glatzel, P.; Van Silfhout, R.; Kachatkou, A.; Bras, W.; Lamberti, C., XAS and XES techniques shed light on the dark side of Ziegler-Natta catalysts: active sites generation. *ChemCatChem* **2015,** *7* (9), 1432–1437.
(48) Groppo, E.; Seenivasan, K.; Gallo, E.; Sommazzi, A.; Lamberti, C.; Bordiga, S., Activation and In Situ Ethylene Polymerization on Silica-Supported Ziegler-Natta Catalysts. *ACS Catal.* **2015,** *5* (9), 5586-5595.
(49) Piovano, A.; Thushara, K. S.; Morra, E.; Chiesa, M.; Groppo, E., Unraveling the Catalytic Synergy between Ti3+ and Al3+ Sites on a Chlorinated Al2O3: A Tandem Approach to Branched Polyethylene. *Angew. Chem. Int. Ed.* **2016,** *55* (37), 11203-11206.
(50) Piovano, A.; Morra, E.; Chiesa, M.; Groppo, E., Tuning the Ti3+ and Al3+ Synergy in an Al2O3/TiClx Catalyst to Modulate the Grade of the Produced Polyethylene. *ACS Catal.* **2017,** *7* (8), 4915-4921.
(51) Piovano, A.; Pletcher, P.; Velthoen, M. E. Z.; Zanoni, S.; Chung, S.-H.; Bossers, K.; Jongkind, M. K.; Fiore, G.; Groppo, E.; Weckhuysen, B. M., Genesis of MgCl2-based Ziegler-Natta Catalysts as Probed with Operando Spectroscopy. *ChemPhysChem* **2018,** *19* (20), 2662-2671.
(52) Kissin, Y. V.; Liu, X.; Pollick, D. J.; Brungard, N. L.; Chang, M., Ziegler-Natta catalysts for propylene polymerization: Chemistry of reactions leading to the formation of active centers. *J. Mol. Catal. A: Chem.* **2008,** *287* (1), 45-52.
(53) Amakawa, K.; Sun, L.; Guo, C.; Hävecker, M.; Kube, P.; Wachs, I. E.; Lwin, S.; Frenkel, A. I.; Patlolla, A.; Hermann, K.; Schlögl, R.; Trunschke, A., How Strain Affects the Reactivity of Surface Metal Oxide Catalysts. *Angew. Chem. Int. Ed.* **2013,** *52* (51), 13553-13557.
(54) Cavalleri, M.; Hermann, K.; Knop-Gericke, A.; Hävecker, M.; Herbert, R.; Hess, C.; Oestereich, A.; Döbler, J.; Schlögl, R., Analysis of silica-supported vanadia by X-ray absorption spectroscopy: Combined theoretical and experimental studies. *J. Catal.* **2009,** *262* (2), 215-223.
(55) Gross, E.; Somorjai, G. A., Molecular catalysis science: Nanoparticle synthesis and instrument development for studies under reaction conditions. *J. Catal.* **2015,** *328*, 91-101.
(56) Escudero, C.; Salmeron, M., From solid–vacuum to solid–gas and solid–liquid interfaces: In situ studies of structure and dynamics under relevant conditions. *Surf. Sci.* **2013,** *607*, 2-9.
(57) Ryo, T.; Hiroshi, K., In-situ observations of catalytic surface reactions with soft x-rays under working conditions. *J. Phys.: Condens. Matter* **2015,** *27* (8), 083003.
(58) Latham, K. G.; Dose, W. M.; Allen, J. A.; Donne, S. W., Nitrogen doped heat treated and activated hydrothermal carbon: NEXAFS examination of the carbon surface at different temperatures. *Carbon* **2018,** *128*, 179-190.
(59) Giorgianni, G.; Mebrahtu, C.; Schuster, M. E.; Large, A. I.; Held, G.; Ferrer, P.; Venturini, F.; Grinter, D.; Palkovits, R.; Perathoner, S.; Centi, G.; Abate, S.; Arrigo, R., Elucidating the mechanism of the CO2 methanation reaction over Niâ€“Fe hydrotalcite-derived catalysts via surface-sensitive in situ XPS and NEXAFS. *Phys. Chem. Chem. Phys.* **2020,** *22* (34), 18788-18797.

(60) Signorile, M.; Braglia, L.; Crocellà, V.; Torelli, P.; Groppo, E.; Ricchiardi, G.; Bordiga, S.; Bonino, F., Titanium Defective Sites in TS-1: Structural Insights by Combining Spectroscopy and Simulation. *Angew. Chem. Int. Ed.* **2020,** *59* (41), 18145-18150.
(61) Fracchia, M.; Ghigna, P.; Pozzi, T.; Anselmi Tamburini, U.; Colombo, V.; Braglia, L.; Torelli, P., Stabilization by Configurational Entropy of the Cu(II) Active Site during CO Oxidation on Mg0.2Co0.2Ni0.2Cu0.2Zn0.2O. *J. Phys. Chem. Lett.* **2020,** *11* (9), 3589-3593.
(62) Braglia, L.; Fracchia, M.; Ghigna, P.; Minguzzi, A.; Meroni, D.; Edla, R.; Vandichel, M.; Ahlberg, E.; Cerrato, G.; Torelli, P., Understanding Solid–Gas Reaction Mechanisms by Operando Soft X-Ray Absorption Spectroscopy at Ambient Pressure. *J. Phys. Chem. C* **2020,** *124* (26), 14202-14212.
(63) Terano, M.; Soga, H.; Kimura, K. Catalyst for Polymerization of Olefins. US 4,829,037, 1989.
(64) Castán-Guerrero, C.; Krizmancic, D.; Bonanni, V.; Edla, R.; Deluisa, A.; Salvador, F.; Rossi, G.; Panaccione, G.; Torelli, P., A reaction cell for ambient pressure soft x-ray absorption spectroscopy. *Rev. Sci. Instr.* **2018,** *89* (5), 054101.
(65) Simonne, D. H.; Martini, A.; Signorile, M.; Piovano, A.; Braglia, L.; Torelli, P.; Borfecchia, E.; Ricchiardi, G., THORONDOR: a software for fast treatment and analysis of low-energy XAS data. *J. Synchrotron Rad.* **2020,** *27* (6), 1741-1752.
(66) Thomas, A.; Fischer, A.; Goettmann, F.; Antonietti, M.; Müller, J.-O.; Schlögl, R.; Carlsson, J. M., Graphitic carbon nitride materials: variation of structure and morphology and their use as metal-free catalysts. *J. Mater. Chem.* **2008,** *18* (41), 4893-4908.
(67) Neese, F., Software update: the ORCA program system, version 4.0. *WIREs Comput. Mol. Sci.* **2018,** *8* (1), e1327.
(68) Takasao, G.; Wada, T.; Thakur, A.; Chammingkwan, P.; Terano, M.; Taniike, T., Machine Learning-Aided Structure Determination for TiCl4–Capped MgCl2 Nanoplate of Heterogeneous Ziegler–Natta Catalyst. *ACS Catalysis* **2019,** *9* (3), 2599-2609.
(69) Becke, A. D., A new mixing of Hartree-Fock and local density-functional theories. *J. Chem. Phys.* **1993,** *98*, 1372-1377.
(70) Lee, C.; Yang, W.; Parr, R. G., Development of the Colle-Salvetti correlation-energy formula into a functional of the electron density. *Phys. Rev. B* **1988,** *37*, 785-789.
(71) Weigend, F.; Ahlrichs, R., Balanced basis sets of split valence, triple zeta valence and quadruple zeta valence quality for H to Rn: Design and assessment of accuracy. *Phys. Chem. Chem. Phys.* **2005,** *7* (18), 3297-3305.
(72) Corradini, P.; Barone, V.; Fusco, R.; Guerra, G., A POSSIBLE MODEL OF CATALYTIC SITES FOR THE STEREOSPECIFIC POLYMERIZATION OF ALPHA-OLEFINS ON 1ST-GENERATION AND SUPPORTED ZIEGLER-NATTA CATALYSTS. *Gazz. Chim. Ital.* **1983,** *113* (9-10), 601-607.
(73) Monaco, G.; Toto, M.; Guerra, G.; Corradini, P.; Cavallo, L., Geometry and stability of titanium chloride species adsorbed on the (100) and (110) cuts of the MgCl2 support of the heterogeneous Ziegler-Natta catalysts. *Macromolecules* **2000,** *33* (24), 8953-8962.
(74) D'Amore, M.; Credendino, R.; Budzelaar, P. H. M.; Causá, M.; Busico, V., A periodic hybrid DFT approach (including dispersion) to MgCl2-supported Ziegler–Natta catalysts – 1: TiCl4 adsorption on MgCl2 crystal surfaces. *J. Catal.* **2012,** *286*, 103−110.
(75) D'Amore, M.; Thushara, K. S.; Piovano, A.; Causà, M.; Bordiga, S.; Groppo, E., Surface Investigation and Morphological Analysis of Structurally Disordered MgCl2 and MgCl2/TiCl4 Ziegler–Natta Catalysts. *ACS Catal.* **2016,** *6* (9), 5786–5796.
(76) Taniike, T.; Terano, M., Coadsorption model for first-principle description of roles of donors in heterogeneous Ziegler-Natta propylene polymerization. *J. Catal.* **2012,** *293*, 39-50.
(77) Shetty, S., Synergistic, reconstruction and bonding effects during the adsorption of internal electron donors and TiCl4 on MgCl2 surface: A periodic-DFT investigation. *Surf. Sci.* **2016,** *653*, 55-65.
(78) Iijima, T.; Shimizu, T.; Goto, A.; Deguchi, K.; Nakai, T.; Ohashi, R.; Saito, M., 47,49Ti solid-state NMR and DFT study of Ziegler-Natta catalyst: Adsorption of TiCl4 molecule onto the surface of MgCl2. *J. Phys. Chem. Solids* **2019,** *135*, 109088.
(79) Grimme, S., A simplified Tamm-Dancoff density functional approach for the electronic excitation spectra of very large molecules. *J. Chem. Phys.* **2013,** *138* (24), 244104.

(80) Roemelt, M.; Neese, F., Excited States of Large Open-Shell Molecules: An Efficient, General, and Spin-Adapted Approach Based on a Restricted Open-Shell Ground State Wave function. *J. Phys. Chem. A* **2013,** *117* (14), 3069-3083.
(81) van Wüllen, C., Molecular density functional calculations in the regular relativistic approximation: Method, application to coinage metal diatomics, hydrides, fluorides and chlorides, and comparison with first-order relativistic calculations. *J. Chem. Phys.* **1998,** *109* (2), 392-399.
(82) Casarin, M.; Finetti, P.; Vittadini, A.; Wang, F.; Ziegler, T., Spin−Orbit Relativistic Time-Dependent Density Functional Calculations of the Metal and Ligand Pre-Edge XAS Intensities of Organotitanium Complexes: TiCl4, Ti(η5-C5H5)Cl3, and Ti(η5-C5H5)2Cl2. *J. Phys. Chem. A* **2007,** *111* (24), 5270-5279.
(83) Note that the Ti loading is different in the three pre-catalysts.
(84) Figgis, B. N., *Introduction to ligand fields*. John Wiley & Sons: New York, 1966.
(85) Molloy, K. C., 9 - Octahedral Complexes. In *Group Theory for Chemists (Second Edition)*, Molloy, K. C., Ed. Woodhead Publishing: 2013; pp 97-108.
(86) Jorgersen, C. K., *Absorption spectra and chemical bonding in complexes.* Pergamon Press: 1962.
(87) Brisdon, B. J.; Lester, T. E.; Walton, R. A., Complex halides of transition metals—III electronic absorption spectra of hexahalotitanates(IV), vanadates(IV), and zirconates(IV). *Spectrochim. Acta A* **1967,** *23* (7), 1969-1976.
(88) de Groot, F. M. F.; Fuggle, J. C.; Thole, B. T.; Sawatzky, G. A., 2p x-ray absorption of 3d transition-metal compounds: An atomic multiplet description including the crystal field. *Phys. Rev. B* **1990,** *42* (9), 5459-5468.
(89) De Groot, F. M. F.; Fuggle, J. C.; Thole, B. T.; Sawatzky, G. A., L2,3 x-ray-absorption edges of d0 compounds: K+, Ca2+, Sc3+, and Ti4+ in Oh (octahedral) symmetry. *Phys. Rev. B* **1990,** *41* (2), 928-937.
(90) Leapman, R. D.; Grunes, L. A.; Fejes, P. L., Study of the L23 edges in the 3d transition metals and their oxides by electron-energy-loss spectroscopy with comparisons to theory. *Phys. Rev. B* **1982,** *26* (2), 614-635.
(91) Note that NEXAFS spectroscopy is not sensitive to the non-equivalence of the Cl centered molecular orbitals (pointed out by UV-Vis spectroscopy), but it gives a deeper insight on the Ti(deg) orbitals, whose transitions were almost out of the spectral range explored by UV-Vis spectroscopy.
(92) Zhao, X.; Zhang, Y.; Song, Y.; Wei, G., XPS study of interaction of titanium species with different internal electron donors on Z–N catalysts. *Surf. Rev. Lett.* **2007,** *14* (05), 951-955.
(93) Jorgensen, C. K., *Halogen Chemistry*. Academic Press: New York, 1967; Vol. 1.
(94) Jorgensen, C. K., Electron Transfer Spectra. *Progr. Inorg. Chem.* **1970,** *12*, 101-157.
(95) Lukens, W. W.; Smith, M. R.; Andersen, R. A., A π-Donor Spectrochemical Series for X in (Me5C5)2TiX, and β-Agostic Interactions in X = Et and N(Me)Ph. *J. Am. Chem. Soc.* **1996,** *118* (7), 1719-1728.
(96) Atkins, P.; Overton, T.; Rourke, J.; Weller, M.; Armstrong, F., *Shriver and Atkins' Inorganic Chemistry*. 5th ed.; Oxford University Press: New York, 2010; p 824.
(97) Clark, R. J. H., Diffuse Reflectance Spectra of Some Anhydrous Transition-Metal Halides. *J. Chem. Soc.* **1964,** *0*, 417-425.
(98) Baldini, G.; Pollini, I.; Spinolo, G., Optical Properties of α- and β-TiCl3. *Phys. Stat. Sol.* **1968,** *27* (1), 95-100.
(99) Pollini, I., Electronic transitions in alpha and beta titanium trichloride. *Solid State Commun.* **1983,** *47* (5), 403-408.
(100) Stoyanov, E.; Langenhorst, F.; Steinle-Neumann, G., The effect of valence state and site geometry on Ti L3,2 and O K electron energy-loss spectra of TixOy phases. *American Mineralogist* **2007,** *92* (4), 577-586.
(101) Henderson, G. S.; Liu, X.; Fleet, M. E., A Ti L-edge X-ray absorption study of Ti-silicate glasses. *Phys. Chem. Minerals* **2002,** *29* (1), 32-42.
(102) Martino, G. A.; Barzan, C.; Piovano, A.; Budnyk, A.; Groppo, E., Tracking the reasons for the peculiarity of Cr/Al2O3 catalyst in ethylene polymerization. *J. Catal.* **2018,** *357*, 206-212.
(103) Allouche, F.; Klose, D.; Gordon, C. P.; Ashuiev, A.; Wörle, M.; Kalendra, V.; Mougel, V.; Copéret, C.; Jeschke, G., Low-Coordinated Titanium(III) Alkyl—Molecular and Surface—Complexes: Detailed Structure from Advanced EPR Spectroscopy. *Angew. Chem. Int. Ed.* **2018,** *57* (44), 14533-14537.

(104) Ashuiev, A.; Allouche, F.; Wili, N.; Searles, K.; Klose, D.; Copéret, C.; Jeschke, G., Molecular and supported Ti(iii)-alkyls: efficient ethylene polymerization driven by the π-character of metal–carbon bonds and back donation from a singly occupied molecular orbital. *Chem. Sci.* **2021,** *12* (2), 780-792.
(105) Morra, E.; Giamello, E.; Van Doorslaer, S.; Antinucci, G.; D'Amore, M.; Busico, V.; Chiesa, M., Probing the coordinative unsaturation and local environment of Ti3+ sites in an activated high-yield Ziegler-Natta catalyst. *Angew. Chem. Int. Ed.* **2015,** *54* (16), 4857-4860.
(106) Ashuiev, A.; Humbert, M.; Gajan, D.; Norsic, S.; Blahut, J.; Searles, K.; Klose, D.; Lesage, A.; Pintacuda, G.; Raynaud, J.; Monteil, V.; Copéret, C.; Jeschke, G., Spectroscopic Signature and Structure of Active Centers in Ziegler-Natta Polymerization Catalysts revealed by Electron Paramagnetic Resonance. *ChemRxiv* **2020**.